

Structural, Kinetic, and Docking Studies of Artificial Imine Reductases Based on Biotin–Streptavidin Technology: An Induced Lock-and-Key Hypothesis

Victor Muñoz Robles,^{†,||} Marc Dürrenberger,^{‡,||} Tillmann Heinisch,[§] Agustí Lledós,[†] Tilman Schirmer,[§] Thomas R. Ward,^{*,‡} and Jean-Didier Maréchal^{*,†}

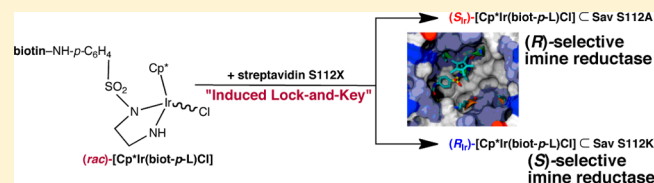
[†]Departament de Química, Universitat Autònoma de Barcelona, Edifici C.n., 08193 Cerdanyola del Vallès, Barcelona, Spain

[‡]University of Basel, Spitalstrasse 51, CH-4056 Basel, Switzerland

[§]Biozentrum, University of Basel, Klingelbergstrasse 50/70, CH-4056 Basel, Switzerland

Supporting Information

ABSTRACT: An artificial imine reductase results upon incorporation of a biotinylated Cp*Ir moiety (Cp* = C₅Me₅[−]) within homotetrameric streptavidin (Sav) (referred to as Cp*Ir(Biot-*p*-L)Cl) C Sav). Mutation of S112 reveals a marked effect of the Ir/streptavidin ratio on both the saturation kinetics as well as the enantioselectivity for the production of salsolidine. For [Cp*Ir(Biot-*p*-L)Cl] C S112A Sav, both the reaction rate and the selectivity (up to 96% ee (*R*)-salsolidine, k_{cat} 14–4 min^{−1} vs [Ir], K_M 65–370 mM) decrease upon fully saturating all biotin binding sites (the ee varying between 96% ee and 45% ee *R*). In contrast, for [Cp*Ir(Biot-*p*-L)Cl] C S112K Sav, both the rate and the selectivity remain nearly constant upon varying the Ir/streptavidin ratio [up to 78% ee (*S*)-salsolidine, k_{cat} 2.6 min^{−1}, K_M 95 mM]. X-ray analysis complemented with docking studies highlight a marked preference of the S112A and S112K Sav mutants for the S_{Ir} and R_{Ir} enantiomeric forms of the cofactor, respectively. Combining both docking and saturation kinetic studies led to the formulation of an enantioselection mechanism relying on an “induced lock-and-key” hypothesis: the host protein dictates the configuration of the biotinylated Ir-cofactor which, in turn, by and large determines the enantioselectivity of the imine reductase.

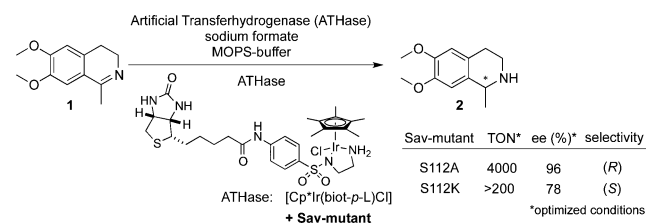


INTRODUCTION

Artificial metalloenzymes result from the incorporation of a catalytically competent organometallic moiety within a macromolecule.^{1–13} Thus far, three anchoring strategies have been pursued to ensure localization of the abiotic cofactor within a well-defined second coordination sphere environment:¹⁴ covalent, dative, or supramolecular. One of the most attractive features of such systems results from combining both chemical and genetic optimization strategies. In this context, the biotin–streptavidin technology has provided a propitious playground for the creation and optimization of artificial metalloenzymes.^{1,15–18} Tethering a biotin anchor to a catalyst precursor ensures that, in the presence of streptavidin (Sav hereafter), the metal moiety is quantitatively incorporated within the host protein. Importantly, the dimer of dimers nature of the Sav homotetramer provides two ideally sized biotin-binding vestibules, each capable of accommodating (up to) two biotinylated catalysts as well as the corresponding substrates. However, as the biotin-binding vestibule is fairly shallow, upon incorporation, the biotinylated catalyst tends to be poorly localized, as reflected by the low metal occupancy in the corresponding X-ray structures.^{19–22} This ill-defined cofactor localization, combined with the vast genetic optimization potential, offers an opportunity but also a challenge for rational structure-based design.

We recently reported on an artificial imine reductase, asymmetric transfer hydrogenase (ATHase hereafter), resulting from incorporation of a biotinylated Cp*Ir-moiety within streptavidin ([Cp*Ir(Biot-*p*-L)Cl] C Sav hereafter) (Cp* = C₅Me₅[−], Scheme 1). We showed that, upon substituting Sav Ser112 with either an alanine or a lysine (i.e., S112A or S112K), both enantiomers of salsolidine **2** could be produced in 96% ee (*R*)- and 78% ee (*S*)-configuration, respectively (Scheme 1).^{21,23} This single-point mutation thus leads to a difference in transition state Gibbs energy $\delta\Delta G^\ddagger = 3.5$ kcal·mol^{−1} between both enantiomers at room temperature.²⁴ Herein, we present

Scheme 1. Artificial Imine Reductase (ATHase) for the Production of Both Enantiomers of Salsolidine **2**



Received: August 20, 2014

Published: October 15, 2014

our efforts to rationalize the effect of point mutations on the structure and catalytic performance of both ATHases.

RESULTS AND DISCUSSION

Michaelis–Menten Behavior of ATHase. In order to gain insight on the kinetics of the two ATHases, we set out to determine the saturation kinetics and the corresponding enantioselectivity for both $[\text{Cp}^*\text{Ir}(\text{Biot-}p\text{-L})\text{Cl}] \subset \text{S112A}$ and $[\text{Cp}^*\text{Ir}(\text{Biot-}p\text{-L})\text{Cl}] \subset \text{S112K}$ at various Ir/Sav ratios. In previous screening studies, we typically set this ratio to 2. The fully loaded X-ray structure of $[\text{Cp}^*\text{Ir}(\text{Biot-}p\text{-L})\text{Cl}] \subset \text{S112A}$ (PDB code 3PK2)²¹ suggests that the four biotinylated cofactors are arranged as two pairs with the Cp^* moieties of each pair within van der Waals contact. We thus speculated that the Ir loading (i.e., Ir/Sav ratio) may have a significant influence on the catalytic performance of the ATHase.²⁵ The Michaelis–Menten behavior and enantioselectivity were determined in triplicate at four different Ir/Sav ratios (1, 2, 3, and 4 vs tetrameric streptavidin) for both S112A and S112K ATHase as well as for the bare catalyst $[\text{Cp}^*\text{Ir}(\text{Biot-}p\text{-L})\text{Cl}]$. The data is displayed in Figure 1 and collected in Table 1.

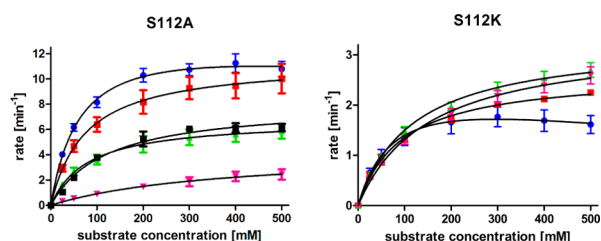


Figure 1. Saturation kinetics profiles of $[\text{Cp}^*\text{Ir}(\text{Biot-}p\text{-L})\text{Cl}] \subset \text{S112A}$ (left) and $[\text{Cp}^*\text{Ir}(\text{Biot-}p\text{-L})\text{Cl}] \subset \text{S112K}$ (right) for the production of salsolidine. The initial rates are displayed with respect to the concentration of iridium. $[\text{Sav}] = 25 \mu\text{M}$ (corresponding to $[\text{biotin binding sites}] = 100 \mu\text{M}$) was held constant, varying the Ir/Sav ratio from 1.0 (blue data points) to 2.0 (red data points), 3.0 (green data points), and 4.0 (magenta data points). For comparison, the initial rates for the free $[\text{Cp}^*\text{Ir}(\text{Biot-}p\text{-L})\text{Cl}]$ catalyst are displayed ($50 \mu\text{M}$, black data points). The black solid lines correspond to the fit obtained either using the Michaelis–Menten or the Haldane equation (see Table 1).

As can be appreciated from these data, the kinetic and selectivity behavior of both ATHases differ markedly. The following trends emerge:

(i) For $[\text{Cp}^*\text{Ir}(\text{Biot-}p\text{-L})\text{Cl}] \subset \text{S112A}$, upon increasing the Ir/Sav ratio beyond 2, the rate decreases (k_{cat} determined vs $[\text{Ir}]$) and the Michaelis constant K_{M} increases. These observations suggest that neighboring $[\text{Cp}^*\text{Ir}(\text{Biot-}p\text{-L})\text{Cl}]$ moieties experience significant steric interaction, leading to a decrease in enzyme–substrate affinity and rate. The modest substrate inhibition (derived from fitting the saturation kinetics behavior with the Haldane equation)²⁶ at Ir/Sav = 1.0 suggests that the biotin-binding vestibule may accommodate the prochiral imine substrate within the empty biotin-binding site. Strikingly, the ee drops sharply to 45% (*R*)-salsolidine **2** at Ir/Sav = 4.0. This suggests that, upon saturating all biotin-binding sites with $[\text{Cp}^*\text{Ir}(\text{Biot-}p\text{-L})\text{Cl}]$, the second coordination sphere environment around the metal, which is responsible for the enantioselection, differs significantly from that at lower Ir/Sav ratios.

(ii) For $[\text{Cp}^*\text{Ir}(\text{Biot-}p\text{-L})\text{Cl}] \subset \text{S112K}$, upon increasing the Ir/Sav ratio, k_{cat} , K_{M} , and ee remain essentially constant. These observations suggest that all four $[\text{Cp}^*\text{Ir}(\text{Biot-}p\text{-L})\text{Cl}]$ moieties operate largely independently, irrespective of the presence or absence of a catalytic moiety in the adjacent biotin-binding site. The substrate inhibition, observed at Ir/Sav = 1.0, is lifted upon increasing the metal loading.

A possible explanation for the striking difference in behavior of the S112A- and S112K-derived ATHases may lie in different binding affinities of the biotinylated cofactor $[\text{Cp}^*\text{Ir}(\text{Biot-}p\text{-L})\text{Cl}]$ for the respective host proteins. Indeed, if only two cofactors bind to S112A with high affinity, one would anticipate an erosion of enantioselectivity upon increasing the Ir:S112A ratio beyond 2. To test this hypothesis, we estimated the binding affinity of $[\text{Cp}^*\text{Ir}(\text{Biot-}p\text{-L})\text{Cl}]$ for both S112A and S112K using the 2-(4-hydroxyphenylazo)benzoic acid (HABA) displacement assay.²⁷ HABA displays millimolar affinity for streptavidin. The resulting host–guest complex HABA \subset Sav exhibits an absorbance at 506 nm. Addition of a biotinylated probe (with higher affinity than HABA) leads to a gradual decrease of the absorbance at $\lambda_{\text{max}} = 506 \text{ nm}$.

This displacement titration procedure was performed with $[\text{Cp}^*\text{Ir}(\text{Biot-}p\text{-L})\text{Cl}]$ using both S112A and S112K. In both cases, the displacement titration curves were nearly identical to those obtained for biotin (see Figure S11, Supporting Information). Most importantly, they reached a minimum at ca. 4.0 equiv, unambiguously demonstrating that up to four $[\text{Cp}^*\text{Ir}(\text{Biot-}p\text{-L})\text{Cl}]$ cofactors have similar affinities for both S112A and S112K. Unfortunately, the linear profiles of the displacement assay precluded a precise determination of the

Table 1. Michaelis–Menten Parameters and Enantioselectivity for the Production of Salsolidine 2 Using Artificial ATHase

entry	Sav mutant	eq $[\text{Ir}]^a$	ee ^c	$k_{\text{cat}}/[\text{Ir}]$ (min^{-1}) ^{d,e}	K_{M} (mM) ^d	K_{I} (mM) ^d
1	no Sav	– ^b	0	8 ± 0.41	120 ± 18	0
2	S112A	1.0	93	14.1 ± 1.7	65 ± 16	3201 ± 3015
3		2.0	92	11.4 ± 0.7	74 ± 17	0
4		3.0	89	6.8 ± 0.5	80 ± 19	0
5		4.0	45	4.3 ± 1.1	370 ± 175	0
6	S112 K	1.0	–70	2.7 ± 0.83	82 ± 47	1073 ± 1138
7		2.0	–74	2.6 ± 0.08	95 ± 9	0
8		3.0	–76	3.3 ± 0.13	119 ± 14	0
9		4.0	–78	3.3 ± 0.17	151 ± 21	0

^aEq $[\text{Cp}^*\text{Ir}(\text{biot-}p\text{-L})\text{Cl}]$ versus free biotin binding sites. ^bCorresponds to an $[\text{Cp}^*\text{Ir}(\text{biot-}p\text{-L})\text{Cl}] = 50 \mu\text{M}$, no Sav present. ^cPositive values correspond to (*R*)-salsolidine **2**, negative values correspond to (*S*)-salsolidine **2**. ^dErrors represent standard errors derived from triplicate measurements. ^e k_{cat} determined vs $[\text{Ir}]$.

affinity. Such a linear profile, however, sets a lower limit for the affinity constant (i.e., $K_a > 10^9 \text{ M}^{-1}$) and thus ensures that >99% of the cofactor is bound to either S112A or S112K at full saturation.

Taken together, these results suggest that the second coordination sphere around S112K ATHase differs significantly from that of the S112A mutant. With the X-ray structure of this latter mutant at hand, we set out to structurally characterize $[\text{Cp}^*\text{Ir}(\text{Biot-}p\text{-L})\text{Cl}] \subset \text{S112K}$ by X-ray crystallography.

X-ray Structure of $[\text{Cp}^*\text{Ir}(\text{Biot-}p\text{-L})\text{Cl}] \subset \text{S112K}$. Crystals of complex $[\text{Cp}^*\text{Ir}(\text{Biot-}p\text{-L})\text{Cl}] \subset \text{S112K Sav}$ were obtained by the soaking technique at pH 8.0, and diffraction data were collected at the synchrotron to 2.5 Å resolution. Upon refining the streptavidin structure, residual electron density in the $2F_o - F_c$ map remained in the biotin-binding cavity (Figure 2). The anomalous dispersion density map revealed two peaks (4.5 and 4.0 Å) in the vestibule that coincided with two strong peaks in the $F_o - F_c$ omit map (11.5 and 5.4 σ). The density was modeled with the $[\text{Cp}^*\text{Ir}(\text{Biot-}p\text{-L})\text{Cl}]$ cofactor in two

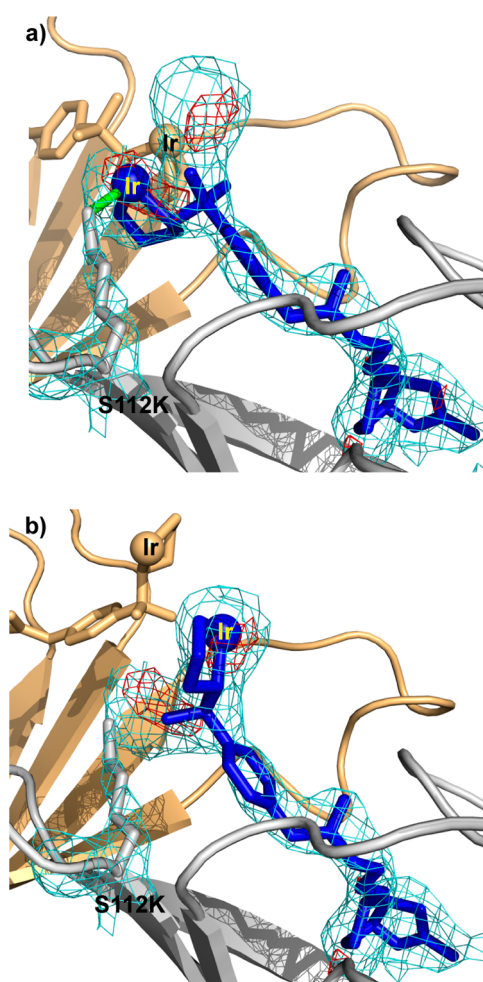


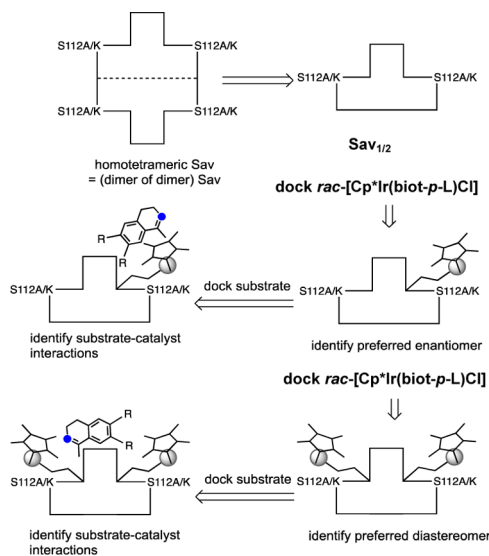
Figure 2. Close-up view of the cofactor conformations A (a) and B (b) in stick-representation modeled into the biotin binding site in the crystal structure of $[\text{Cp}^*\text{Ir}(\text{Biot-}p\text{-L})\text{Cl}] \subset \text{S112K Sav}$ (PDB code 4OKA). Only one Sav dimer (monomers are highlighted in gray and brown, respectively) is depicted for clarity, the Cp^{*-} and Cl^- could not be located and are thus not displayed. The green cylinder highlights the $\text{N}\zeta\text{-Lys112}\cdots\text{Ir}$ contact. The $2F_o - F_c$ electron density and the anomalous difference density map are highlighted in aquamarine and red and are contoured at 1 σ and 2.5 σ , respectively.

conformations (A and B with occupancies of 60% and 40%, respectively) related by a rotation of 180° around the $\text{C}_{\text{benzene}} - \text{S}_{\text{sulfonamide}}$ bond (Figure 2). No electron density for any additional ligands at iridium (e.g., Cp^* , Cl^- or H_2O etc.) could be detected in the $F_o - F_c$ omit map. We hypothesize that this may be due to the flexibility of the cofactor within the shallow biotin-binding vestibule. In the $F_o - F_c$ omit map, no residual electron density was detected to model the side chain of Lys112, suggesting a high flexibility. However, upon modeling its side chain in an extended conformation, electron density became visible in the $2F_o - F_c$ map (Figure 2). In this conformation, the distance $\text{N}\zeta\text{-Lys112}\text{-Ir}$ is 2.3 Å, suggesting a bonding interaction between Ir-N . We assume that the three remaining free coordination sites are occupied by Cp^{*-} , thus suggesting an absolute configuration of the metal of R_{Ir} . Orientation A produced similarities to the cofactor in structure $[\text{Cp}^*\text{Ir}(\text{Biot-}p\text{-L})\text{Cl}] \subset \text{S112A Sav}$ (PDB code 3PK2,²¹ Figure S12a, Supporting Information) while the cofactor conformation B shares similarities with its counterpart in structure $[(\eta^6\text{-benzene})\text{Ru}(\text{Biot-}p\text{-L})\text{Cl}] \subset \text{Sav-S112K}$ (PDB code 2QCB,¹⁹ Figure S12b, Supporting Information).

Unfortunately, the absence of the substrate in the crystal structure and the apparent flexibility of both the cofactor and the lysine 112, as well as the lack of Cp^* and Cl^- densities, do not allow one to establish a molecular relationship for the ee and rates observed for both mutants. We thus turned to docking simulations to gain further structural insight.

Docking Simulations. In order to analyze the kinetic- and ee profiles, several molecular features of the ATHase were addressed by computational means, as summarized in Scheme 2: (i) Do Sav S112A and Sav S112K have any preference for binding $[\text{Cp}^*\text{Ir}(\text{Biot-}p\text{-L})\text{Cl}]$ in a given absolute configuration at the metal? (ii) What is the complementarity between the cofactor and the substrate? (iii) What is the influence of the occupation of one biotin binding site on the catalytic profile of the adjacent cofactor?

Scheme 2. Stepwise Docking Strategy Used To Identify (i) Enantiodiscrimination between a Model Dimeric Streptavidin Sav_{1/2} and (rac)- $[\text{Cp}^*\text{Ir}(\text{Biot-}p\text{-L})\text{Cl}]$ and (ii) Critical Interactions between the ATHase and the Prochiral Imine Substrate



To address these questions, a stepwise computational process was performed. Calculations were first carried out for S112A and S112K with a single biotinylated catalyst $[\text{Cp}^*\text{Ir}(\text{Biot-}p\text{-L})\text{Cl}]$ per Sav dimer (Sav_{1/2} hereafter: Sav is best described as a dimer of dimers with two close-lying biotin binding sites) with either (*R*_{Ir})- or (*S*_{Ir})-metal configuration. In a second step, an additional $[\text{Cp}^*\text{Ir}(\text{Biot-}p\text{-L})\text{Cl}]$ moiety, either with an (*R*_{Ir})- or an (*S*_{Ir})-configuration, was docked in the host dimer model for both S112A Sav_{1/2} and S112K Sav_{1/2}. At both stages, the dihydroisoquinoline substrate **1** was docked to identify how the prochiral substrate may reach a reactive location in the various ATHases (Scheme 2). The dockings were performed with allowing full flexibility of the iridium complex. For the S112K mutant, the lysine was also allowed to freely move using a library of rotameric states.²⁸ Finally, in order to study the possible coordination between Lys112 and the iridium atom upon binding, dockings were performed first using an pseudoatom type implemented in GOLD and simulating an electron deficient metal and then optimizing the best energy complexes using the QM/MM approach ONIOM-(PBE:AMBER) with an extended basis set and a flexible binding sphere of out 10 Å around the metal center.³⁰

Identification of the Preferred Metal Configuration for $[\text{Cp}^*\text{Ir}(\text{Biot-}p\text{-L})\text{Cl}]$ in S112A Sav. Despite the absence of density for the Cp* and the Cl⁻ of the organometallic cofactor, the X-ray structure of $[\text{Cp}^*\text{Ir}(\text{Biot-}p\text{-L})\text{Cl}]$ in S112A²¹ suggests the presence of a diastereopure complex, (*S*_{Ir})- $[\text{Cp}^*\text{Ir}(\text{Biot-}p\text{-L})\text{Cl}]$, snugly embedded within Sav S112A. Because a “racemic at iridium” biotinylated cofactor was used for soaking the Sav crystals, this result implies an enantiodiscrimination by the protein environment on the metal center. In order to better ascertain this configurational preference, (*R*_{Ir})- and (*S*_{Ir})-pseudoenantiomers were docked within S112A Sav_{1/2} (see the Supporting Information). The lowest energy orientations for the (*S*_{Ir})- and (*R*_{Ir})-moieties were predicted to have good binding affinities (about 40 scoring units) with a slight preference for the (*S*_{Ir})-metal over the (*R*_{Ir})-cofactor (no more than 1.2 scoring units; see Table 2). However, this preference may be higher than predicted by the pure scoring function. Indeed, analysis of the energetic breakdown of both binding modes shows a clear preference for *S*_{Ir} in absolute energetic terms ΔG (about 5 kJ·mol⁻¹ as reported in Table SI2,

Table 2. Summary of the Docking Results of the Pseudoenantiomers of $[\text{Cp}^*\text{Ir}(\text{Biot-}p\text{-L})\text{Cl}]$ Catalyst in the S112A and S112K Sav

host protein	cofactor config	score ^a	RMSD ^b (Å)
S112A	<i>S</i> _{Ir}	44.4	1.0
	<i>R</i> _{Ir}	43.2	2
S112 K	<i>S</i> _{Ir}	51.5	1.7 ^A
	<i>R</i> _{Ir}	58.6	1.4 ^A
<i>(S</i> _{Ir})- $[\text{Cp}^*\text{Ir}(\text{Biot-}p\text{-L})\text{Cl}]$ in S112A	<i>S</i> _{Ir}	43.1	1.3
	<i>R</i> _{Ir}	43.9	3.2
<i>(R</i> _{Ir})- $[\text{Cp}^*\text{Ir}(\text{Biot-}p\text{-L})\text{Cl}]$ in S112K	<i>S</i> _{Ir}	42.5	2.8 ^B
	<i>R</i> _{Ir}	44.4	3.0 ^B

^aScores correspond to dimensionless ChemScore values as established in GOLD.^{29,34} ^bRoot mean square deviations (RMSD) for lowest energy docking solution vs X-ray structures. For S112K, the RMSD values are for the experimental binding modes that present the best structural overlap with conformer A (indicated by A) and with conformer B (indicated by B).

Supporting Information). Only corrective terms associated with internal degrees of freedoms penalize this binding mode, something for which scoring functions are currently not accurate for organometallic compounds (i.e., no relaxation of the first coordination sphere upon binding).²⁹

The most stable binding modes of the cofactor in the $[\text{Cp}^*\text{Ir}(\text{Biot-}p\text{-L})\text{Cl}]$ in S112A structure were superposed with the X-ray structure.²¹ The resulting RMSD is 1.0 and 2.0 Å for *S*_{Ir} and *R*_{Ir}, respectively [Figures SI3a (Supporting Information) and 3a]. Both energetic and RMSD considerations suggest that the (*S*_{Ir})-metal center better fits the protein vestibule.

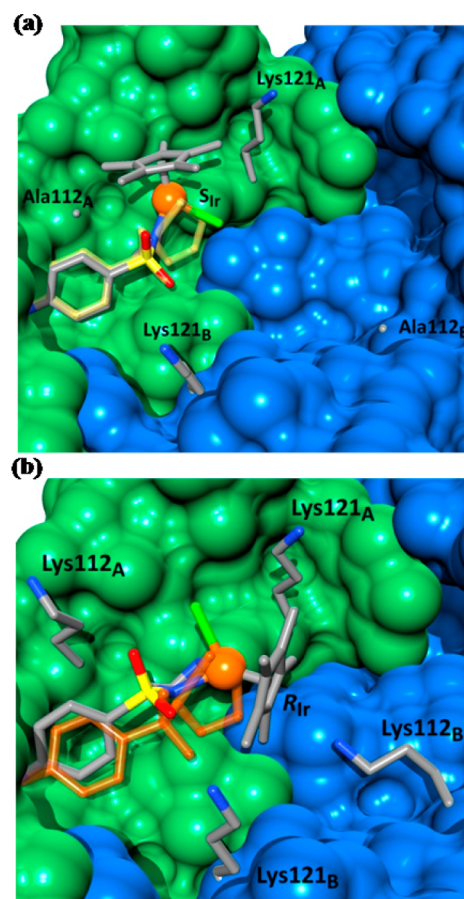


Figure 3. Representation of the lowest-energy orientation obtained for the docking for the preferred pseudoenantiomers in both the S112A (*(S*_{Ir})- $[\text{Cp}^*\text{Ir}(\text{Biot-}p\text{-L})\text{Cl}]$, top) and the S112K mutants (*(R*_{Ir})- $[\text{Cp}^*\text{Ir}(\text{Biot-}p\text{-L})\text{Cl}]$, bottom). Monomers A and B are depicted in green and blue, respectively. For comparison, the crystallographically determined position of the cofactors is highlighted as yellow and orange ghost structures in the S112A and S112K models, respectively (in the latter case only conformation A is depicted for clarity).

To understand how this complementarity could impact the enantioselectivity observed experimentally, docking of the imine **1** substrate was performed on both (*R*_{Ir})- and (*S*_{Ir})-cofactor-loaded streptavidin. The conformational search was restrained to a reasonable distance for hydride transfer with all the remaining degrees of freedom entirely allowed. It is important to mention that the chloride was substituted by its corresponding hydride in those calculations, hence leading to an inversion of the configuration at the metal by virtue of the Cahn–Ingold–Prelog priorities: (*S*_{Ir})- $[\text{Cp}^*\text{Ir}(\text{Biot-}p\text{-L})\text{Cl}]$ becomes (*R*_{Ir})- $[\text{Cp}^*\text{Ir}(\text{Biot-}p\text{-L})\text{H}]$. The best docked structures

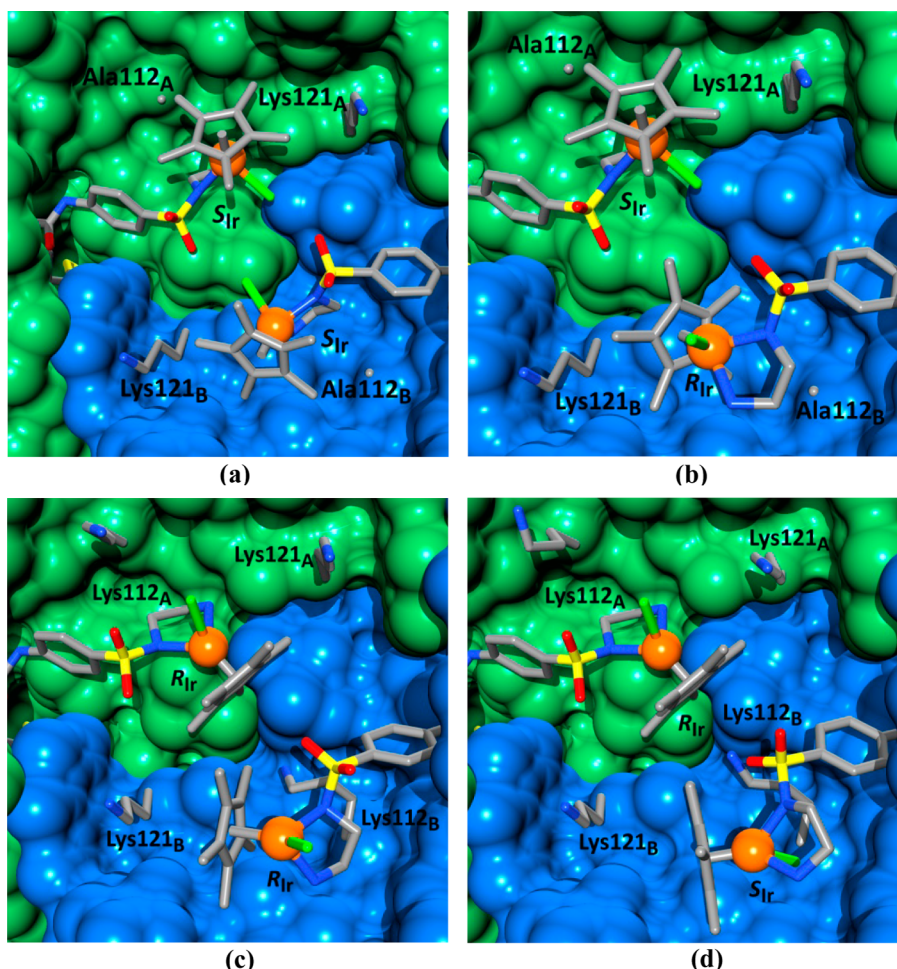


Figure 4. Representation of the models of a fully loaded dimer of the Sav tetramer. Most relevant residues are in stick representation. Monomer A is depicted in green and monomer B in blue. Top: Mutant S112A with two (S_{Ir})-[Cp*Ir(Biot-*p*-L)Cl] cofactors (a) or one (S_{Ir})- and one (R_{Ir})-[Cp*Ir(Biot-*p*-L)Cl] (b). Bottom: Mutant S112K with two (R_{Ir})-[Cp*Ir(Biot-*p*-L)Cl] cofactors (c) or one (R_{Ir})- and one (S_{Ir})-[Cp*Ir(Biot-*p*-L)Cl] (d).

for the (R_{Ir})-[Cp*Ir(Biot-*p*-L)H] \subset S112A reveals substrate **1** located deep inside the opposite biotin binding cavity (Figure S13a, Supporting Information), while the same calculation for (S_{Ir})-[Cp*Ir(Biot-*p*-L)H] \subset S112A leads to a highly solvent exposed prochiral imine **1** with limited interactions with surface residues of the host protein, a situation unlikely to provide the highly enantioenriched product **2** (Figure S13b, Supporting Information).

Taken together, the docking studies suggest that with a unique cofactor loaded monomer per dimer of S112A the reaction proceeds via an (R_{Ir})-[Cp*Ir(Biot-*p*-L)H] \subset S112A Sav to afford highly enantioenriched (*R*)-salsolidine **2**. These observations are consistent with the experimental results, thus giving us confidence to model the [Cp*Ir(Biot-*p*-L)H] \subset S112K ATHase.

Identification of the Preferred Metal Configuration for [Cp*Ir(Biot-*p*-L)Cl] \subset S112K Sav. The above methodology was applied to analyze the ATHase derived from the S112K Sav mutant, considering both the (R_{Ir})- and (S_{Ir})-[Cp*Ir(Biot-*p*-L)Cl] cofactor configurations. Calculations were first performed with a coordinatively saturated metal (i.e., no coordination with amino acid side chains).

For both pseudoenantiomers, the lowest energy binding modes of the biotinylated catalyst fit well with the conformation A observed in the X-ray structure (Table 2).

The predicted lowest energy binding modes for the (S_{Ir})- and (R_{Ir})-[Cp*Ir(Biot-*p*-L)Cl] cofactors were 51.5 and 58.6 score units, respectively, thus suggesting that the (R_{Ir})-pseudoenantiomer is energetically favored (Table 2 and Figure 3b).

As suggested by the X-ray data, we further explored the ability of Lys112 to coordinate the iridium metal by reproducing in silico this phenomenon. To this end, and because of the need to account for the formation of a coordination bond, we applied an integrative protocol suited to simulate interactions between organometallic cofactors and protein residues, a feature absent from usual protein–ligand docking approaches.³⁰

A protein–ligand docking with optimized parameters for treating metals with a vacant coordination site allied with QM/MM refinements (see the Supporting Information) suggests that Lys112 can interact only with the cofactor leading to an (S_{Ir})-configuration upon coordination (resulting from Cl[−] substitution from (R_{Ir})-[Cp*Ir(Biot-*p*-L)Cl]). The QM/MM simulation confirmed an Ir–Lys112_A contact with an Ir–N $\zeta_{Lys112A}$ distance of 2.2 Å. The calculated RMSD between the QM/MM-minimized structure and the A conformation in the S112K X-ray structure is 0.8 Å, suggesting that the experimental orientation is compatible with a coordination of the catalyst by Lys112_A (Figure S14, Supporting Information).

Interestingly, the dockings with and without direct interaction between $N_{\zeta_{Lys112A}}$ and the metal led to nearly overlapping orientations (RMSD 0.7 Å). This suggests that the coordination of the lysine to the metal is not determinant in fixing the orientation of the cofactor within the binding site but likely that an equilibrium exists in solution between bound and unbound iridium center. At this stage, however, none of the docking solutions led to the alternative conformation B of the cofactor as identified in the X-ray structure.

To decipher the influence of the absolute metal configuration of the cofactor in determining the catalytic environment, the dihydroisoquinoline **1** was docked on both (R_{Ir}) - and (S_{Ir}) - $[Cp^*Ir(Biot-p-L)H] \subset S112K$ ATHases (Figure S13c,d, Supporting Information). The results show that the substrate is challenged to reach the hydride only in the (R_{Ir}) - $[Cp^*Ir(Biot-p-L)H]$ configuration (Figure S13c, Supporting Information). We thus hypothesize that the (S_{Ir}) - $[Cp^*Ir(Biot-p-L)H] \subset S112K$ is the preferred metal configuration, both in terms of stability and activity. However, protein–ligand dockings are not accurate enough to predict the enantioselectivity for the reduction process. Simulations involving quantum mechanical based techniques and a wide exploration of the precatalytic state of the enzyme would be needed for this purpose.

Taken together, this first part of the computational analysis of the ATHases suggests that S112K and S112A mutants stabilize different pseudoenantiomers of the embedded catalyst. This in turn offers different second coordination sphere environments for the approach of the substrate **1**. For the homogeneous transfer-hydrogenation catalyst pioneered by Noyori and co-workers, the critical role of the chirality at the metal is well-documented:^{31,32} the enantiopure aminosulfonamide ligand enforces one configuration at the metal that, in turn, dictates which prochiral face of the substrate can approach the hydride to afford the preferred enantiomer of the product. In the present case, we hypothesize that the host protein influences the enantiodiscriminating step in a similar way: incorporation of a configurationally labile piano stool moiety³³ $[Cp^*Ir(Biot-p-L)Cl]$ within the host protein favors one configuration at the metal: (S_{Ir}) - $[Cp^*Ir(Biot-p-L)Cl] \subset S112A$ and (R_{Ir}) - $[Cp^*Ir(Biot-p-L)Cl] \subset S112K$. This by and large dictates which enantiomer of salsolidine **2** is produced. Additional interactions between the substrate and the host protein contribute to fine-tune the enantioselectivity, eventually leading to salsolidine **2** in up to 96% ee *R* and 78% ee *S* for S112A and S112K ATHases, respectively.

Structural Consequences of Increasing the Ir/Sav Ratio in $[Cp^*Ir(Biot-p-L)Cl] \subset S112A$ and S112K. Additional docking simulations were performed on (S_{Ir}) - $[Cp^*Ir(Biot-p-L)Cl] \subset S112A$ to identify how a second cofactor may affect the structure and the corresponding activity of the fully loaded Sav_{1/2} (which in turn helps rationalize the mechanism of the fully loaded tetrameric Sav). Both the (S_{Ir}) - and the (R_{Ir}) -cofactors were docked in the second pocket of Sav_{1/2} (Figure 4a,b). The small difference in scores (Table 2) shows that there is no significant chiral discrimination for the binding of the second cofactor. Inspection of the structure reveals that for the (S_{Ir},S_{Ir}) -system, both chlorides point toward each other with a short Cl–Cl distance (3.8 Å) (Figure 4a). In this configuration, there is little space for the dihydroisoquinoline **1** to approach the catalyst. Therefore, it is expected that the fully loaded (S_{Ir},S_{Ir}) - $[Cp^*Ir(Biot-p-L)Cl]_2 \subset S112A$ ATHase displays limited activity (Figure S15a, Supporting Information). In

stark contrast, in the (S_{Ir},R_{Ir}) - $[Cp^*Ir(Biot-p-L)Cl]_2 \subset S112A$, the (R_{Ir}) -cofactor better fits into the adjacent cavity offering its chloride face accessible for the substrate. However, the Cp^* ligand of this same catalyst impedes the access of the substrate **1** to the hydride of the adjacent (S_{Ir}) -enantiomer, thus eroding the activity rate of the Sav_{1/2} [Figures 4b and S15b (Supporting Information)].

Protein–ligand dockings were also performed with (S_{Ir}) - and (R_{Ir}) -metal cofactors on the (R_{Ir}) - $[Cp^*Ir(Biot-p-L)Cl] \subset S112K$ model. Although little energy differences were observed (Table 2), structural differences were substantial (Figure 4c). The (R_{Ir},R_{Ir}) - $[Cp^*Ir(Biot-p-L)Cl]_2 \subset S112K$ hybrid presented both chlorides facing the Lys112 of the same monomer where the biotinylated cofactor is bound, whereas in the R_{Ir},S_{Ir} combination the docked (S_{Ir}) -cofactor has its chloride facing the interface of the two monomers (Figure 4d). Docking calculations with the dihydroisoquinoline **1** substrate in both hybrids revealed that in the R_{Ir},R_{Ir} case, each monomer is active and behaves independently with no interaction between the adjacent cofactors (Figure S15c, Supporting Information), while in the R_{Ir},S_{Ir} model, only the (R_{Ir}) -cofactor embedded monomer should be catalytically active, as the substrate is challenged to reach the (S_{Ir}) -cofactor (Figure S15d, Supporting Information). Therefore, only the (R_{Ir},R_{Ir}) - $[Cp^*Ir(Biot-p-L)Cl]_2 \subset S112K$ model is consistent with the experimental data gathered for the S112K ATHase, where a nearly constant rate irrespective of the number of Ir equivalents (Table 1) is observed. Those results are essentially unaltered when considering the possibility of Lys112 to coordinate to the iridium center. Those calculations actually predict that two homogeneous catalysts could bind the same Sav_{1/2} dimer, each one of them interacting with a different Lys112. We hypothesize that the Ir–lysine interactions might favor the rapid epimerization of the piano stool moiety during the catalytic cycle. More insight on the regeneration of the catalyst through the use of formic acid would be needed and should answer whether this contact has a role in the catalytic cycle or it is just an artifact created by the crystallization conditions.

Interestingly, in most calculations of the (R_{Ir},R_{Ir}) - $[Cp^*Ir(Biot-p-L)Cl]_2 \subset S112K$ model with or without the metal coordinated by Lys112, low-energy solutions present the second cofactor in a binding mode closer to orientation B, with some of them reaching an RMSD < 1 Å. Since this binding mode is absent in the simulations performed for the binding of the first cofactor, these results suggest that a B-like conformation could be stabilized when the adjacent monomer is loaded. This suggests that the two monomers of a fully loaded dimer present a mixture of A and B-like orientations and have different second coordination sphere environments for the metal. Simulations to reproduce two cofactors with an orientation B as it stands in the X-ray structure lead to no enantioselectivity for the metal center by the protein scaffold [both (R_{Ir}) - and (S_{Ir}) -enantiomers of the cofactors have similar binding energies]. In the resulting orientations, the chloride is systematically exposed to the solvent and neither the chirality of the metal nor the contacts of the protein in its second coordination sphere can help rationalize the enantioselectivity observed experimentally.

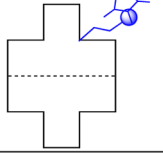
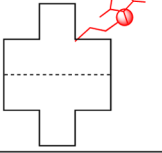
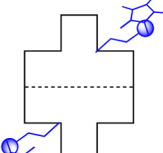
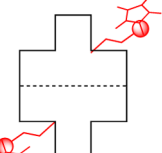
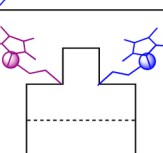
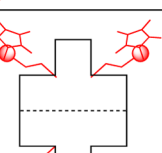
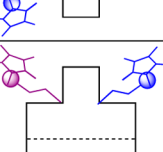
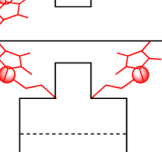
For both cofactors, the respective protein environment surrounding the substrate docked in the (R_{Ir},R_{Ir}) - $[Cp^*Ir(Biot-p-L)Cl]_2 \subset S112K$ hybrid are slightly different, and in both cases, the prochiral imine is exposed to the solvent. This suggests that the enantioselection is by and large dictated by

the chirality at the metal rather than second coordination sphere interactions between the prochiral imine and the protein. This contrasts with (S_{Ir}) -[Cp*Ir(Biot-*p*-L)Cl] \subset S112A, where the substrate **1** is surrounded by a protein cavity, thus contributing to fine-tune the enantioselectivity (up to 96% ee)

CONCLUSION AND OUTLOOK

Combining structural and kinetic data with the docking simulations, the following mechanistic insights can be inferred for the ATHases (Table 3).

Table 3. Phenomenological Rationalization of the Rate and Enantioselectivity of ATHase as a Function of Ir/Sav Ratio and Mutant^a

S112A		S112K	
Equivalents of cofactor	ee Rate	Equivalents of cofactor	ee Rate
	Max. Max.		Max. Max.
	Max. Max.		Max. Max.
	Max. Decreases		Max. Max.
	Decreases Decreases		Max. Max.

^aBlue, red, and violet cofactors symbolize (S_{Ir}) -[Cp*Ir(Biot-*p*-L)Cl], (R_{Ir}) -[Cp*Ir(Biot-*p*-L)Cl], and (rac) -[Cp*Ir(Biot-*p*-L)Cl], respectively.

1. [Cp*Ir(Biot-*p*-L)Cl] \subset S112A. (i) The first cofactor binds with an (S_{Ir}) -configuration of the metal (Figure 3a). In this situation the system reaches its maximum rate and highest enantioselectivity (Table 1, entry 2). Relying on a QM/MM study, we recently analyzed the subtle details of enantioselection for this system, highlighting the critical involvement of Lys121 in stabilizing the substrate via cation- π interactions.²³

(ii) On the basis of the above docking studies, we anticipate that the second cofactor binds to the opposite dimer of the tetrameric streptavidin, thus minimizing clashes between the

two cofactors. In this situation, we predict a combination of two (S_{Ir}) -[Cp*Ir(Biot-*p*-L)Cl] \subset S112A dimeric units forming an ATHase operating at the same rate (vs [Ir]) and yielding similar enantioselectivities (Table 3). This prediction is largely verified experimentally (Table 1, entry 3).

(iii) No enantiopreference is predicted for the binding of a third cofactor within Sav S112A (Figure 4a,b). Due to close contacts between the adjacent catalysts, the substrate is challenged to reach the hydride in the (S_{Ir},S_{Ir}) -Sav_{1/2} and only in the (S_{Ir},R_{Ir}) -hybrids it could reach the (R_{Ir}) -cofactor in a solvent-exposed way. In this situation the performance of the ATHase should be negatively affected and the observed activity and selectivity for [Cp*Ir(Biot-*p*-L)Cl]₃ \subset S112A can thus be generally traced back to the singly occupied Sav_{1/2} (Table 1, entry 4).

(iv) As in point iii, fully loading the four biotin binding sites leads to [Cp*Ir(Biot-*p*-L)Cl]₄ \subset S112A with significantly eroded rate and selectivity (Table 1, entry 5).

2. [Cp*Ir(Biot-*p*-L)Cl] \subset S112K. The docking studies performed on the S112K ATHase suggest that the first and second catalysts bound to the homotetrameric Sav are in an (R_{Ir}) -configuration (Figure 4c). Importantly and in stark contrast to the S112A ATHase, all four biotin-binding sites can accommodate an (R_{Ir}) -[Cp*Ir(Biot-*p*-L)Cl] cofactor. In this situation, each catalytic event is by and large confined within one monomer and thus little affected by the Sav:Ir ratio. However, the substrate **1** is highly solvent exposed with limited contacts with the protein environment. A nearly constant rate (vs [Ir]) and enantioselectivity are thus predicted, irrespective of the Ir/Sav ratio. These predictions are largely corroborated experimentally (Table 1, entries 5–9). The localization the cofactor is close enough to Lys112 so that this residue can interact with the metal. However, the absence of clear density and the relatively little impact of this coordination on the geometry of the system suggest a transient structure that rapidly converts to catalytically competent systems.

Considering that the ATHases derived from S112A and S112K mutants afford opposite enantiomers, we suggest that it is the absolute configuration at Ir which for the most part determines the preferred enantiomer of the reduction product. This situation may be viewed as an “induced lock-and-key” fit, whereby the second coordination sphere provided by the Sav mutant induces an enantiopure configuration at the metal center which, in turn, governs to which prochiral face of the substrate the hydride is delivered. Subtle substrate–protein interactions further contribute to fine-tune the enantioselectivity.

It is gratifying that, despite the qualitative nature of the docking simulations, the kinetic and structural data all in all corroborate the predictions. Current efforts are aimed at producing a heterotetrameric Sav with only two functional biotin-binding sites and engineering additional weak interactions between the substrate and the host protein.

ASSOCIATED CONTENT

Supporting Information

Material and methods for kinetics measurements and crystallography protocol and resolution, as well as details on the molecular modeling tools and procedure followed; Tables S11 and S12 for X-ray data collection and extended docking analysis, respectively; and figures associated with HABA displacement titration (Figure S11), binding site comparison between cofactor-loaded Sav mutants S112A and S112K

(Figure SI2), docking solutions of $[\text{Cp}^*\text{Ir}(\text{Biot-}p\text{-L})\text{H}]$ interacting with substrate for Sav_{1/2} mutants (Figure SI3), depiction of the doubly occupied S112K Sav_{1/2} ATHase (Figure SI4) with the Lys112 coordinated to the metal center and representation of the models of a fully loaded dimer of the Sav tetramer (Figure SI5). This material is available free of charge via the Internet at <http://pubs.acs.org>.

AUTHOR INFORMATION

Corresponding Authors

thomas.ward@unibas.ch.

JeanDidier.Marechal@uab.cat.

Author Contributions

[†]V.M.R. and M.D. contributed equally to this work.

Notes

The authors declare no competing financial interest.

ACKNOWLEDGMENTS

T.R.W. thanks Umicore for a loan of $[\text{Cp}^*\text{IrCl}_2]_2$, Prof. C. Cantor for the streptavidin gene, and Prof. K. Faber for suggesting the “induced lock-and-key” term. Generous funding was provided by the SNF (grant 200020_144354) and the Cantons of Basel and the Swiss Nanoscience Institute. Financial support from the Spanish Ministerio de Economía y Competitividad (Project CTQ2011-23336) is acknowledged. V.M.R. is grateful to the Spanish MINECO for a FPI Fellowship.

REFERENCES

- (1) Wilson, M. E.; Whitesides, G. M. *J. Am. Chem. Soc.* **1978**, *100*, 306–307.
- (2) Levine, H. L.; Kaiser, E. T. *J. Am. Chem. Soc.* **1978**, *100*, 7670–7677.
- (3) Qi, D.; Tann, C.-M.; Haring, D.; Distefano, M. D. *Chem. Rev.* **2001**, *101*, 3081–3112.
- (4) Köhler, V.; Wilson, Y. M.; Lo, C.; Sardo, A.; Ward, T. R. *Curr. Opin. Biotechnol.* **2010**, *21*, 744–752.
- (5) Reetz, M. T. *Top. Organomet. Chem.* **2009**, 63–92.
- (6) Jing, Q.; Okrasa, K.; Kazlauskas, R. J. *Top. Organomet. Chem.* **2009**, 45–61.
- (7) Jing, Q.; Okrasa, K.; Kazlauskas, R. J. *Chem. An Eur. J.* **2009**, *15*, 1370–1376.
- (8) Ueno, T.; Abe, S.; Yokoi, N.; Watanabe, Y. *Coord. Chem. Rev.* **2007**, *251*, 2717–2731.
- (9) Mayer, C.; Gillingham, D. G.; Ward, T. R.; Hilvert, D. *Chem. Commun.* **2011**, *47*, 12068–12070.
- (10) Lu, Y.; Yeung, N.; Sieracki, N.; Marshall, N. M. *Nature* **2009**, *460*, 855–862.
- (11) Boersma, A. J.; Megens, R. P.; Feringa, B. L.; Roelfes, G. *Chem. Soc. Rev.* **2010**, *39*, 2083–2092.
- (12) Rosati, F.; Roelfes, G. *ChemCatChem* **2010**, *2*, 916–927.
- (13) Fournier, P.; Fiammengio, R.; Jäschke, A. *Angew. Chem. Int. Ed.* **2009**, *48*, 4426–4429.
- (14) Steinreiber, J.; Ward, T. R. *Coord. Chem. Rev.* **2008**, *252*, 751–766.
- (15) Ward, T. R. *Acc. Chem. Res.* **2011**, *44*, 47–57.
- (16) Lin, C.-C.; Lin, C.-W.; Chan, A. S. C. *Tetrahedron: Asymmetry* **1999**, *10*, 1887–1893.
- (17) Hyster, T. K.; Knörr, L.; Ward, T. R.; Rovis, T. *Science* **2012**, *338*, 500–503.
- (18) Podtetenieff, J.; Taglieber, A.; Bill, E.; Reijerse, E. J.; Reetz, M. T. *Angew. Chem. Int. Ed.* **2010**, *122*, 5277–5281.
- (19) Creus, M.; Pordea, A.; Rossel, T.; Sardo, A.; Letondor, C.; Ivanova, A.; Letrong, I.; Stenkamp, R. E.; Ward, T. R. *Angew. Chem. Int. Ed.* **2008**, *47*, 1400–1404.
- (20) Zimbron, J. M.; Sardo, A.; Heinisch, T.; Wohlschlager, T.; Gradinaru, J.; Massa, C.; Schirmer, T.; Creus, M.; Ward, T. R. *Chem. An Eur. J.* **2010**, *16*, 12883–12889.
- (21) Dürrenberger, M.; Heinisch, T.; Wilson, Y. M.; Rossel, T.; Nogueira, E.; Knörr, L.; Mutschler, A.; Kersten, K.; Zimbron, M. J.; Pierron, J.; Schirmer, T.; Ward, T. R. *Angew. Chem. Int. Ed.* **2011**, *50*, 3026–3029.
- (22) Zimbron, J. M.; Heinisch, T.; Schmid, M.; Hamels, D.; Nogueira, E. S.; Schirmer, T.; Ward, T. R. *J. Am. Chem. Soc.* **2013**, *135*, 5384–5388.
- (23) Muñoz Robles, V.; Vidossich, P.; Lledós, A.; Ward, T. R.; Maréchal, J.-D. *ACS Catal.* **2014**, *4*, 833–842.
- (24) Balcells, D.; Maseras, F. *New J. Chem.* **2007**, *31*, 333–343.
- (25) As the biotin-binding event is essentially noncooperative, a statistical distribution of $[\text{Cp}^*\text{Ir}(\text{Biot-}p\text{-L})\text{Cl}]$ within Sav is expected upon varying the Ir/Sav ratio from 1 to 4.
- (26) Haldane, J. *Enzymes*; Longman, Green and Co.: New York, 1930.
- (27) Skander, M.; Humbert, N.; Collot, J.; Gradinaru, J.; Klein, G.; Loosli, A.; Sauser, J.; Zocchi, A.; Gilardoni, F.; Ward, T. R. *J. Am. Chem. Soc.* **2004**, *126*, 14411–14418.
- (28) Chase, F.; Avenue, B. *Curr. Opin. Struct. Biol.* **2002**, *12*, 431–440.
- (29) Ortega-Carrasco, E.; Lledós, A.; Maréchal, J.-D.; Ortega Carrasco, E.; Maréchal, J.-D. *J. Comput. Chem.* **2014**, *35*, 192–198.
- (30) Muñoz Robles, V.; Ortega-Carrasco, E.; Fuentes, E. G.; Lledós, A.; Maréchal, J.-D. *Faraday Discuss.* **2011**, *148*, 137.
- (31) Martins, J. E. D.; Clarkson, G. J.; Wills, M. *Org. Lett.* **2009**, *11*, 847–850.
- (32) Yamakawa, M.; Ito, H.; Noyori, R. *J. Am. Chem. Soc.* **2000**, *122*, 1466–1478.
- (33) Ward, T. R.; Schafer, O.; Daul, C.; Hofmann, P. *Organometallics* **1997**, *16*, 3207–3215.
- (34) Verdonk, M. L.; Cole, J. C.; Hartshorn, M. J.; Murray, C. W.; Taylor, R. D. *Proteins: Struct. Funct. Bioinf.* **2003**, *52*, 609–623.